Micro Combustion Chamber: comparison between LES and Experiments

A. Minotti[1], C. Bruno[2] and F. Cozzi[3]
[1,2] *Department of Mechanical & Aeronautical Engineering, University of Rome "La Sapienza"*
Via Eudossiana 18, 00184, Rome, Italy
[1] angelo.minotti@uniroma1.it
[2] claudio.bruno@uniroma1.it
[3] *Politecnico di Milano, Dipartimento di Energia*
Via la Masa 34, Milan, Italy
fabio.cozzi@polimi.it

Abstract

The goal of this paper is to investigate the performance of microcombustors. Such devices are currently under rapid development in particular for propulsion, e.g., for UAVs, and as micro-electrical power generators.
This study focuses on a cylindrical microcombustor fed by methane and air, with diameter and height 0.006m and 0.009m, respectively. It extends previous work performed by these authors using RANS methodology and reduced chemical mechanisms. Here two 3D LES numerical simulations with the flamelet model and the detailed GRIMech 3.0 mechanism is performed, and its results are compared to the experimental data obtained by one of these authors (F.Cozzi). Maximum temperature inside the chamber and at the exhaust section, together with a CH* chemiluminescence's image and a combustion efficiency analysis, are provided. Results show that particular attention must be given to the grid refinement: it is not always true that results improve with refinement.
This work should be seen as an advance in the understanding of how to design, and what to expect from, future microcombustors applications.

1. Introduction

An investigation of the performance of microcombustors applied to microturbines and micropropulsion in general is presented in this paper. The field of ultra-micro thermo-electric/ electronic devices is rapidly developing under the ever growing pressure of new and more stringent requirements posed by the increasing need for portable power generation. In particular, three main areas of interest for micro-combustion exist: propulsion, UAV ("drones") for tactical and meteorological reconnaissance, and portable electrical power generation.
The present numerical simulation work improves on the work in [1], where two FANS numerical simulations (with global and reduced reaction mechanisms) were compared with the experimental data obtained from the microcombustor designed and built at the Polytechnic of Milan. That work defined models to simulate micro-combustion chambers. The study and results reported here were obtained by means of two 3D unsteady LES simulations of fuel-air mixing in a cylindrical micro combustion chamber burning methane and air at 1atm that provides about 125W of thermal power. Simulations differ in the imposed wall temperature.

In this work the dynamic kinetic energy (DKE) subgrid model [2,3] is used to model turbulent transport at the sub-grid scale. In contrast to the usual subgrid scales models (classic [4] or dynamic [5,6] Smagorinsky-Lilly-type models) the DKE does not assume the existence of a local equilibrium range between the transferred energy through the grid-filter scales and the dissipation of kinetic energy at small subgrid scales, and solves an additional subgrid kinetic energy transport equation.

The DKE model requires a higher computational effort, justified by its higher performance in modeling flows with large deformation rates, as in the present geometry: in fact, the [swirling] streamlines curvature is of order 10^3 m^{-1} or more.

The wall treatment by Werner and Wengle [7] provides velocity more accurate than using the classical law of the wall.

Combustion-turbulence coupling is modeled by 57 flamelets [8-15], with kinetics reproduced by the GRIMech3.0 mechanism [16] including 53 species and 325 reactions.

The numerical equations were solved on a 16 Quad-Core Xeon™ processors, each with 16Gb RAM; 0.14s of physical time were simulated vs. a residence time close to 0.002s. A time step of 1×10^{-6}s was adopted. These simulations took almost 70 days of computational time.

Temperature maps, mixing maps and combustion efficiency are reported.

This paper is structured as follows: section 2 provides the combustion chamber description and operating conditions; section 3 discusses turbulence and combustion models. Results are in section 4.

2. Combustion Chamber and Operating Conditions

The combustion chamber geometry and dimensions influence mixing dynamics and, consequently, the combustion efficiency associated to swirl.

The non-premixed meso-scale whirl combustor is shown in Fig. 1, the cylindrical combustion chamber is 0.006 m in diameter and 0.009 m height and it has a volume of about 254 mm^3.

The experimental results have been obtained by using a meso-scale combustor made of Inconel. Tangential air injection generates a swirling flow, while to improve mixing the gaseous fuel was injected tangentially and at 90° with respect to the air flow.

The methane and air ducts diameter is 0.001 m, that of the exhaust is 0.002 m. Fig. 1 shows the micro combustion chamber; Fig.2 the combustion chamber domain, divided into slices. The computational domain consists of 500,000 unstructured cells. Near the wall $y^+<1$ and $\Delta y^+\approx1$, the high stretching level due to the geometry notwithstanding and suggesting results are grid independent [17,18].

Operating and boundary conditions are reported in Table 1. The fuel inlet Reynolds number is in the laminar regime; the Re_{air} is barely turbulent. This feature is characteristic (and peculiar) of microcombustors, hence the importance of an accurate analysis of the Reynolds maps inside the combustion chamber in order to identify and locate laminar zones. This possibility is enhanced by combustion, that tends to laminarize the flow, opposed by the slight expansion inside the chamber; the final regime is determined by the balance and dynamic competition between these two effects.

With these inlet conditions the non-dimensional swirl number, S, defined as the axial flux of swirling momentum divided by the axial flux of axial momentum, times the equivalent nozzle radius is:

$$S = \frac{\int_A \rho u_x u_\theta r dA}{r \int_A \rho u_x^2 dA} = 1.7$$

As for the combustor wall, its temperature was not measured in the experiments. The estimated Biot number, that gives a simple measure of the ratio between heat transfer resistances *inside of* and that *at the interface* between solid wall and gas, is equal to:

$$Bi = \frac{hL_c}{k} = 0.01$$

(*h* is the convective heat transfer coefficient, L_c a characteristic length and *k* is the body thermal conductivity). This value suggests that the solid metal block hosting the combustor cavity may be considered almost isothermal; the temperature measured on the outside surface (see Fig. 1) is about 534K. A simply estimation of the internal wall temperature based on the steady 1D conduction in a axysimmetric body and the measured wall temperature suggested to impose a temperature of 550 K at the internal walls in the "Simulation 1", while "Simulation 2" has been carried out with chamber walls temperature equal to 750K for comparison.

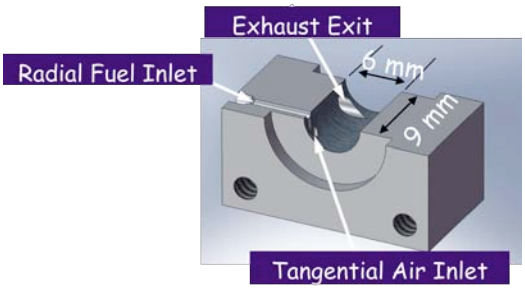

Figure 1 Micro Combustion Chamber

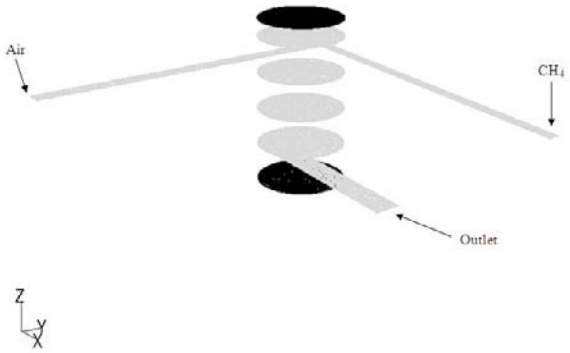

Figure 2 Representative geometry of the micro-combustion chamber

Table 1 Operating and Boundary Conditions

	Methane	Air
Mass Flow Rate [kg/s]	2.46×10^{-6}	6.02×10^{-5}
Inlet Total Temperature [K]	300	303.3
Inlet Density [kg/m3]	0.66	1.2
Outlet Pressure [Pa]	101325	
Wall	No slip condition; 550 K and 750K	
Global equivalence ratio	0.7	
Re	900	4000

3. Turbulence, Combustion and Numerical Models

3.1 Turbulence: Large Eddy Simulation and the Kinetic Energy Sub-Grid Scale Model

The LES approach is used to simulate turbulent transport.
The unknown sub-grid stresses resulting from filtering are modeled by means of the DKE SGS model [2]. This model does not assume equilibrium between energy transferred through the resolved scales and the dissipation of kinetic energy at small grid-scales (an assumption underlying most other algebraic SGS models).
The subgrid kinetic energy is defined by:

$$k_{sgs} = \frac{1}{2}\left(\overline{u_k^2} - \overline{u}_k^2\right) \tag{1}$$

obtained by contracting the SGS stress:

$$\tau_{ij} = \rho\overline{u_i u_j} - \rho\overline{u}_i\overline{u}_j \tag{2}$$

The SGS eddy viscosity, μ_t, is calculated from k_{sgs} as:

$$\mu_t = C_k k_{sgs}^{1/2} \Delta_f \tag{3}$$

where Δ_f is the filter size, and $\Delta_f \equiv V^{1/3}$, with V the cell volume.

The subgrid-scale stress can then be written as:

$$\tau_{ij} - \frac{2}{3} k_{sgs} \delta_{ij} = -2 C_k k_{sgs}^{1/2} \Delta_f \overline{S}_{ij} \tag{4}$$

where $\overline{S}_{ij}$ is the strain tensor for the resolved scale defined by:

$$\overline{S}_{ij} \equiv \frac{1}{2} \left(\frac{\partial \overline{u}_i}{\partial x_j} + \frac{\partial \overline{u}_j}{\partial x_i} \right) \tag{5}$$

and k_{sgs} is obtained by solving its transport equation:

$$\frac{\partial k_{sgs}}{\partial t} + \overline{u}_j \frac{\partial k_{sgs}}{\partial x_j} = -\tau_{ij} \frac{\partial \overline{u}_i}{\partial x_j} - C_\varepsilon \frac{k_{sgs}^{3/2}}{\Delta_f} + \frac{\partial}{\partial x_j} \left(\frac{\mu_t}{\sigma_k} \frac{\partial k_{sgs}}{\partial x_j} \right) \tag{6}$$

In the above equations, the constants C_k and C_ε are determined dynamically [2], while σ_k is hardwired to 1.0.

Beside the dynamic model, the high swirling level imposed by the geometry dictated a particular wall treatment. This is based on the work of Werner and Wengle [6] and on analytical integration of the near-wall power law velocity distribution, resulting in the following expression for the wall shear stress:

$$|\tau_w| = \begin{cases} \dfrac{2\mu |u_p|}{\Delta z} & \text{for} \quad |u_p| \le \dfrac{\mu}{2\rho\Delta z} A^{\frac{2}{1-B}} \\ \rho \left[\dfrac{1-B}{2} A^{\frac{1+B}{1-B}} \left(\dfrac{\mu}{\rho \Delta z} \right)^{1+B} + \dfrac{1+B}{A} \left(\dfrac{\mu}{\rho \Delta z} \right)^{B} |u_p| \right]^{\frac{2}{1+B}} & \text{for} \quad |u_p| \ge \dfrac{\mu}{2\rho\Delta z} A^{\frac{2}{1-B}} \end{cases} \tag{7}$$

where u_p is the velocity parallel to the wall, A=8.3 and B=1/7 are constants, and Δz is the near-wall control volume length scale.

3.2 Combustion: the Flamelet Model

The flamelet model is one of the approaches used in the non-premixed combustion model to account for chemical non-equilibrium. The flamelet concept views the turbulent flame as an ensemble of thin, laminar, locally one-dimensional flamelet structures embedded within the turbulent flow field [9-11]. This non-premixed model allows intermediate (radical) species prediction, dissociation effects, and turbulence-chemistry coupling. It is based on the assumption of equal diffusivities for all the species, generally acceptable for turbulent flows. Even tough in this configuration the inlet Reynolds numbers are low, the 90° impinging jets enhance turbulence and mixing; turbulent convection overwhelms molecular diffusion, so transport properties are approximated here by those of nitrogen, the species with the highest mass fraction.
It follows that the instantaneous thermochemical state of the fluid is related to the mixture fraction $f=(Z_i-Z_{i,ox})/(Z_{i,fuel}-Z_{i,ox})$ [8]. Its corresponding Favre mean conservation equation is:

$$\frac{\partial(\rho\bar{f})}{\partial t}+\nabla\cdot(\rho\vec{v}\bar{f})=\nabla\cdot\left(\frac{\mu_t}{\sigma_t}\nabla\bar{f}\right) \tag{8}$$

By defining $f'=f-\bar{f}$ a second conservation equation, for the mixture fraction variance $\overline{f'^2}$, used in the closure model:

$$\frac{\partial(\rho\overline{f'^2})}{\partial t}+\nabla\cdot(\rho\vec{v}\overline{f'^2})=\nabla\cdot\left(\frac{\mu_t}{\sigma_t}\nabla\overline{f'^2}\right)+C_g\mu_t(\nabla\bar{f})^2-C_d\rho\frac{\varepsilon}{k}\overline{f'^2} \tag{9}$$

Default values were imposed to the constants σ_t, C_g and C_d (0.85, 2.86, and 2.0, respectively).
The chemistry can be reduced and completely described by two quantities, f and $\chi=2D|\nabla f|^2$ (scalar dissipation, [s^{-1}]) [9-12], where D is the turbulent diffusion coefficient. This reduction of complex chemistry to 2 variables allows flamelets to be preprocessed and stored in look-up tables. reducing considerably computational cost.
Since the species mass fractions and temperature in the laminar flamelets are completely parametrized by f and χ_{st}, density-weighted mean species mass fractions and temperature in the turbulent flame can be determined from the PDF of f and χ_{st} as

$$\bar{\phi}=\iint\phi(f,\chi_{st})p(f,\chi_{st})dfd\chi_{st} \tag{10}$$

where Φ is the symbol for species mass fractions and temperature, a β-PDF shape is assumed for f, and a Dirac δ function for χ. A simplified set of the mixture fraction equations are solved [13-14]. N equations must be solved for the N species mass fractions, Y_i,

$$\rho\frac{\partial Y_i}{\partial t}=\frac{1}{2}\rho\chi\frac{\partial^2 Y_i}{\partial f^2}+S_i \tag{11}$$

and one equation for temperature:

$$\rho \frac{\partial T}{\partial t} = \frac{1}{2}\rho\chi \frac{\partial^2 T}{\partial f^2} - \frac{1}{c_p}\sum_i H_i S_i + \frac{1}{2c_p}\rho\chi \left[\frac{\partial c_p}{\partial f} + \sum_i c_{p_i}\frac{\partial Y}{\partial f}\right]\frac{\partial T}{\partial f} \qquad (12)$$

where Y_i, T, ρ, and f are the *i-th* specie mass fraction, temperature, density and mixture fraction, respectively. The c_{pi} and c_p are the *i-th* species specific heat and mixture-averaged specific heat, respectively. S_i is the *i-th* species reaction rate, and H_i is the specific enthalpy of the *i-th* species. The reaction rate depends on the chemical mechanism, here the GRIMech3.0 [16].
The scalar dissipation, χ, across the flamelet, is [15]:

$$\chi(f) = \frac{a_s}{4\pi}\frac{3\left(\sqrt{\rho_\infty/\rho}+1\right)^2}{\left(2\sqrt{\rho_\infty/\rho}+1\right)}\exp\left(-2\left[erfc^{-1}(2f)\right]^2\right) \qquad (13)$$

where ρ_∞ is the density of the oxidizer stream. Note that, compared to larger combustors, swirl and especially curvature of micro-combustors greatly enhance χ.
Here 57 flamelets, defined by the initial scalar dissipation χ=1 and with $\Delta\chi$=1, have been used to model combustion-turbulence coupling.

3.3 Numerical model

The simulation has been carried out with a pressure-based solver using an algorithm belonging to the general class of method called projection method [19].
In this method the constraint of mass conservation (continuity) in the velocity field is achieved by solving a pressure (or pressure correction) equation. This solver uses a solution algorithm where the governing equations are solved sequentially (segregated from one another) [20].
The SIMPLEC (SIMPLE-Consistent algorithm) [21], with a skewness correction (particularly useful with this high-curvature geometry) [22], is used to resolve the pressure-velocity correcting coupled equation; the SIMPLEC uses a relationship between velocity and pressure corrections to enforce mass conservation and to obtain the pressure field.
The unsteady formulation employs a central 2nd order implicit scheme. The momentum equation is discretized by the "bounded central differencing scheme" [23], while the 3rd order MUSCL (Monotone Upstream-Centered Schemes for Conservatives Laws) scheme [24] discretizes the energy and mixture fraction equations: this scheme blends a central difference scheme and a 2nd order upwind scheme.
The pressure equation is discretized by a 2nd order method.

4. Results

Results shown here are obtained after 0.14s of simulated physical time, vs. a residence time of almost 0.002s (the numerical time step is 1×10^{-6}s); note that experimental measurements were taken after 20 min from ignition, in order to reach steady-state.
Figures 3 and 4 show the time averaged temperature inside the chamber for "Simulation 1" (walls at 550K) and the corresponding RMS map.
Figures 5 and 6 show the same but for "Simulation 2" (walls at 750K).
For clarity, slices at 0.001m, 0.003m, 0.005 and at 0.008m are reported; slices at 0.008m and at 0.001m are, respectively, the inlet plane and the outlet plane.
The maximum temperature inside the chamber is 1790K for "Simulation 1" and 1900K for "Simulation 2".
These figures show also that the temperature peaks close to the wall, hence the wall heat fluxes are very large, particularly in the zone near the inlet ducts.
At the exhaust section the predicted temperature is close to 880K and 1120K, respectively for "Simulation 1" and "Simulation 2"; that measured is close to 1150K [25].

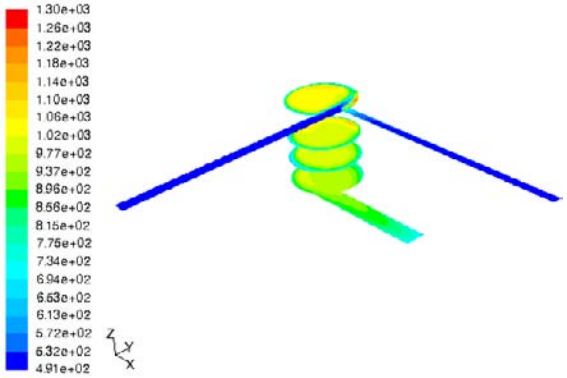

Figure 3 T_{wall} 550K : mean temperature

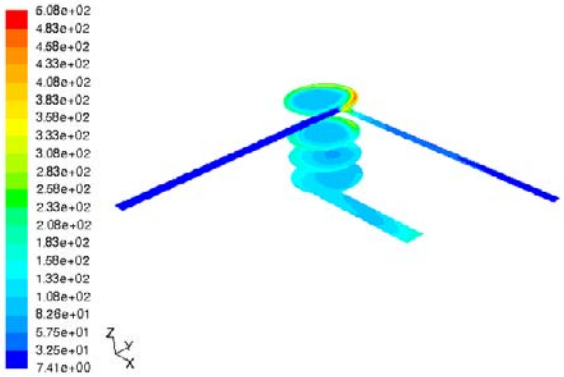

Figure 4 T_{wall} 550K: static temperature RMS map

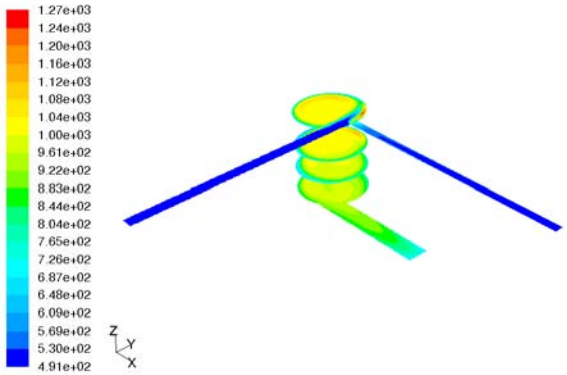

Figure 5 T_{wall} 750K: mean temperature

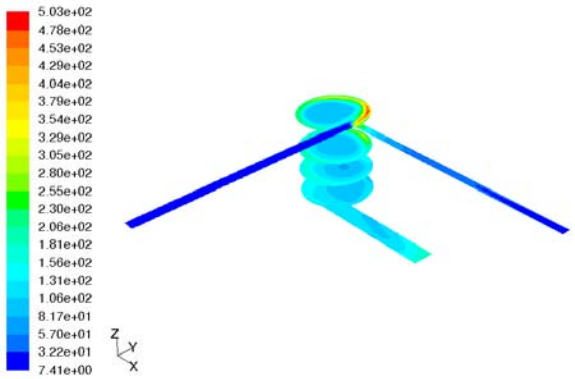

Figure 6 T_{wall} 750K: static temperature RMS map

Table 2 compares simulations and experiments; in particular CO_2, CO and O_2 molar fractions, measured [25] and predicted at the exhaust section ($\chi_i = n_i/(n_{tot} - n_{H2O})$), the exhaust temperature and the combustion efficiency defined as:

$$\eta = \left. \frac{\chi_{CO_2}}{\chi_{CO_2} + \chi_{CO}} \right|_{outlet} \tag{14}$$

Table 2 Simulations vs Experiments: comparison

	Φ	χ_{CO2}	χ_{CO}	χ_{O2}	η	$T_{at\ exit}$
Experiments	0.70	4.1%	1.8%	0,11	0.7	~1150K
Simulation 1, Twall 550K	0.70	7.4%	0.001%	5.15%	0.998	~880K
Simulation 2, Twall 750K	0.70	9.3%	0.089%	1.56%	0.991	~1120K

Table 2 shows how "Simulation 2" predicts a temperature at the exhaust section closer to that measured.

As for species predictions, CO_2 is over-estimated while CO and O_2 are under-estimated in both simulations. The lower than measured CO molar fraction leads to an over-predicted combustion efficiency that in both cases is close to 1 against the measured value of 0.7.

Figures 7-8 show the mean CO and CO_2 mass fraction maps inside the chamber for "Simulation 1" while figures 9-10 are for "Simulation 2".

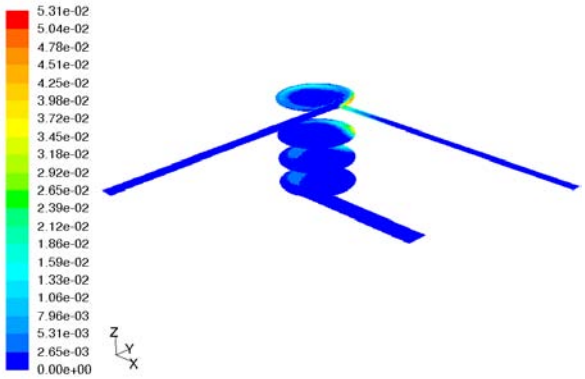

Figure 7 T_{wall} 550K : mean CO mass fraction map

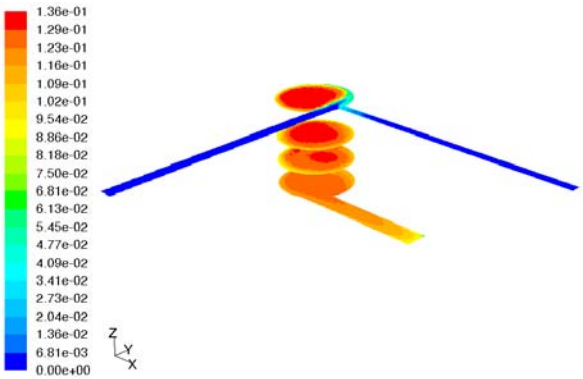

Figure 8 T_{wall} 550K : mean CO_2 mass fraction map

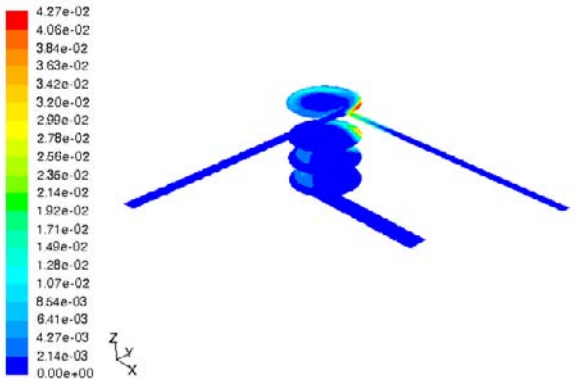

Figure 9 T_{wall} 750K : mean CO mass fraction map

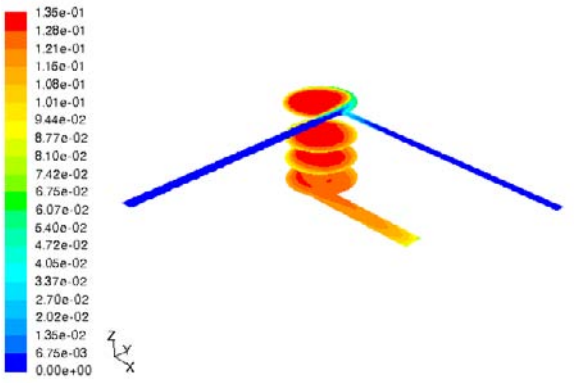

Figure 10 T_{wall} 750K : mean CO_2 mass fraction map

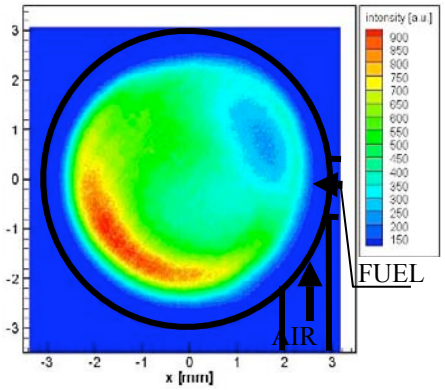

Figure 11 Mean images of CH* chemiluminescence. The internal wall is shown by the black line.

Figure 11 shows the experimental CH* imaging used to analyze the spatial distribution of the local heat release [26]; anyway it should be reminded that these line of sight measurements should be interpreted cautiously [27]. The mean CH* image in figure 11 shows the maximum CH* intensity occurring opposite to the air/fuel injection zone, while the center of the combustor was characterized by a weaker CH* emission, and the region of minimum intensity was located close to the reactant inlets. Due to flame quenching at the wall, no CH* emission was observed there: this 'dead' space had an average thickness of roughly 0.5 mm. Temperature maps obtained by the numerical simulation (figures 3-6) shows a flame, identified by the highest temperature region, located very close to the wall and to the zone of fuel and air jet impingement, just where no CH* emission has been experimentally observed. This result could suggests that the numerical simulation underpredicted the CO molar fraction, see Table 2, as a consequence of a poor prediction of the wall effects on the flame due to the high temperature gradients.

Figure 12-15 report the mean Z-velocity on the planes "XZ" and "YZ". These figures show only negative Z-velocities, consistent with the "in-out direction" trough the chamber; the blank zones (positive Z-velocities) point to wide recirculation bubbles inside the chamber, important for the mixing process.

This flow reversal is brought about by the shape of the geometry, in particular by the outlet section being perpendicular to the cylinder axis and tangent to its external surface (see figs. 1-2, above).

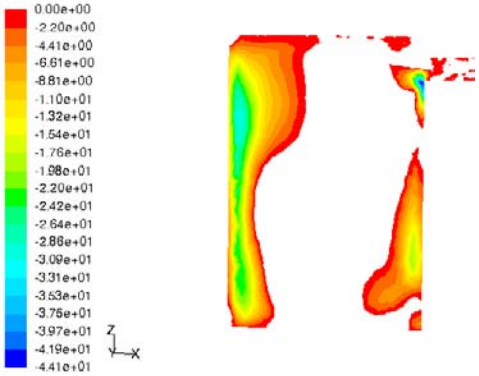

Figure 12 T_{wall} 550K : mean Z-velocity map, XZ plane

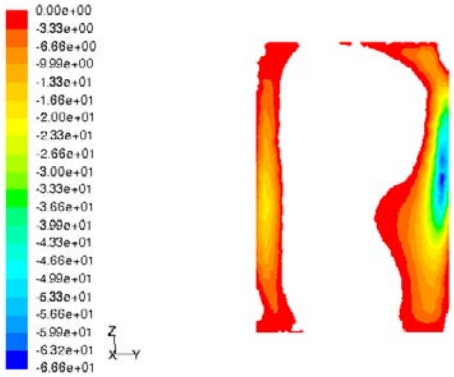

Figure 13 T_{wall} 550K :mean Z-velocity map, YZ plane

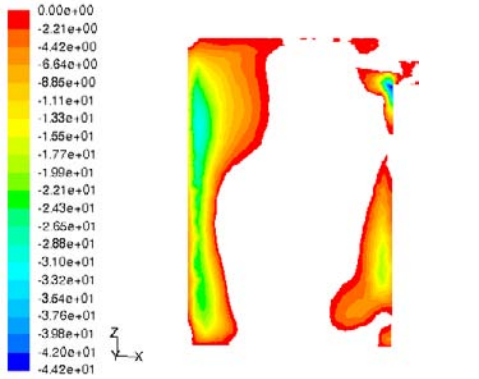

Figure 14 T_{wall} 750K : mean Z-velocity map, XZ plane

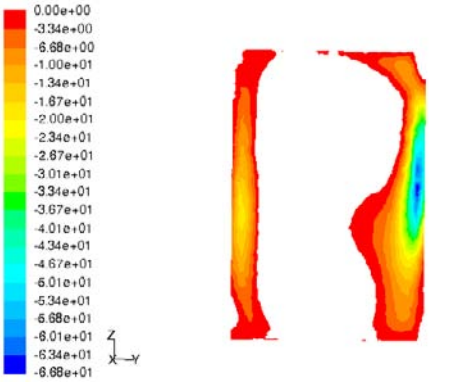

Figure 15 T_{wall} 750K :mean Z-velocity map, YZ plane

Figure 16-19 show the velocity and the RMS velocity maps inside the chamber.
Velocities fluctuations inside the chamber are of the same order of time averaged velocities; this implies that swirling enhances turbulence, as expected, justifying the Flamelet approach for both the simulations, highest values are in the exit duct.

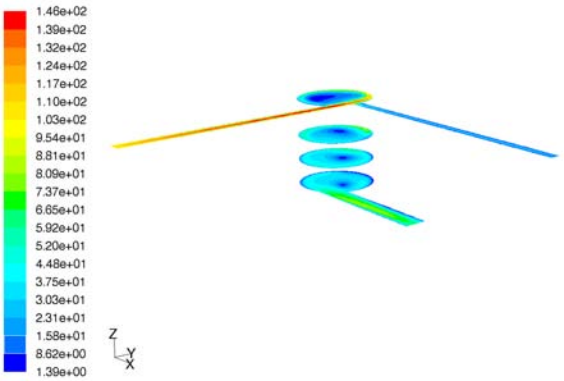

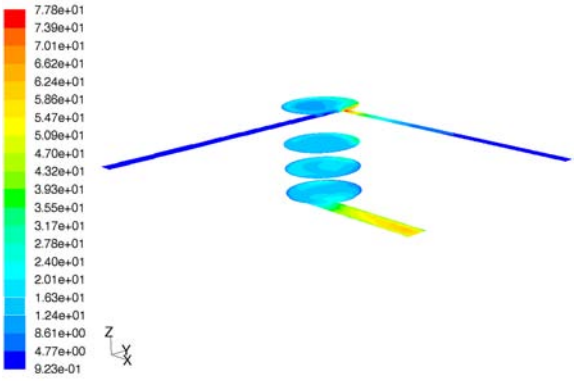

Figure 16 T_{wall} 550K :mean velocity magnitude maps

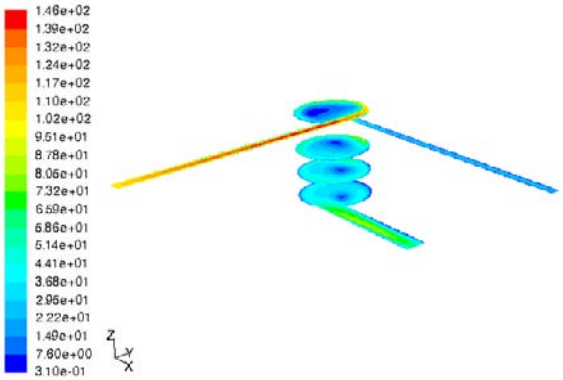

Figure 17 T_{wall} 550K :velocity magnitude RMS maps

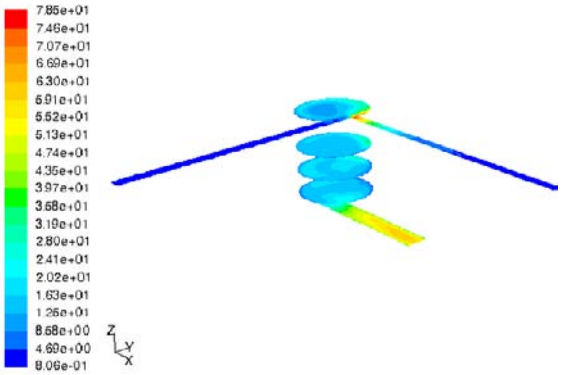

Figure 18 T_{wall} 750K :mean velocity magnitude maps

Figure 19 T_{wall} 750K :velocity magnitude RMS maps

Figures 19 and 22 provide, respectively, the molecular viscosity and the SubGrid turbulent viscosity for the cases at T_{wall}=550K and at T_{wall}=750K.

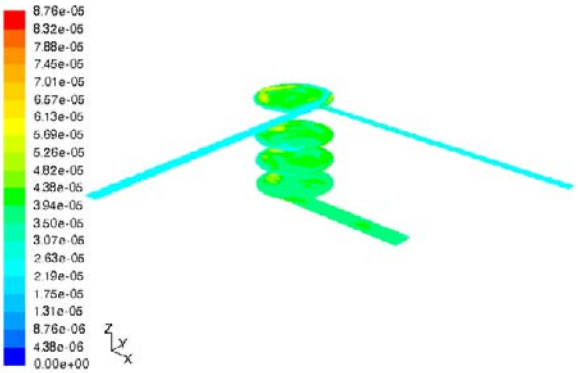

Figure 19 T_{wall} 550K:molecular viscosity

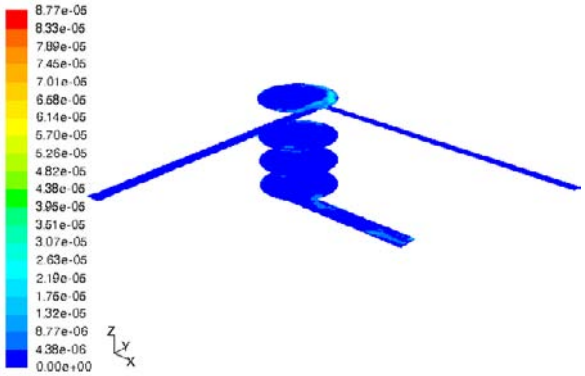

Figure 20 T_{wall} 550K: SubGrid turbulent viscosity

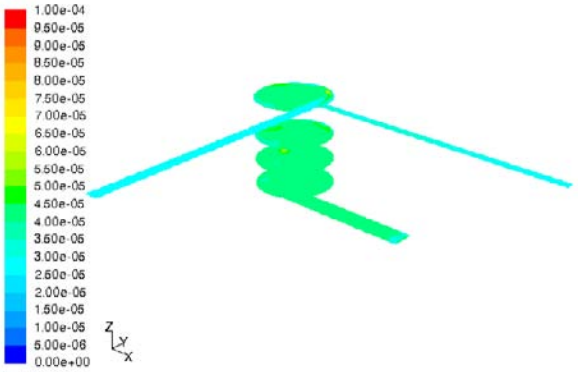

Figure 21 T_{wall} 750K:molecular viscosity

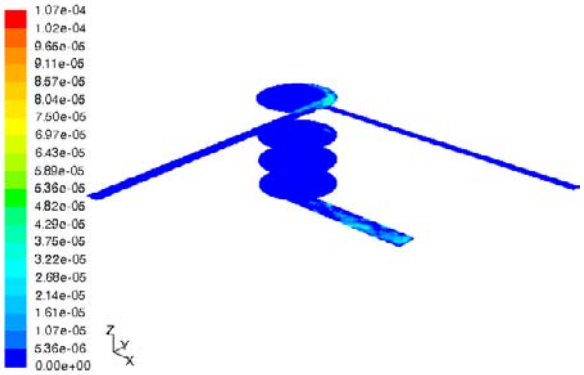

Figure 22 T_{wall} 750K: SubGrid turbulent viscosity

Figures 19-22 show that the turbulent viscosity is everywhere much lower than molecular viscosity: even though the "physical turbulence" inside the chamber is high (figures 16-19 above), justifying the non premixed approach, the "numerical turbulence" is low due to the mesh width (see eq. 3).
A "too low numerical turbulence" badly affects the mixture fraction transport equations (eqs. 8-9), hence equations 11-12 by means of the scalar dissipation "χ" described as function of "f" in equation 14.
Equation 8 shows that a low turbulent viscosity means a small mixture fraction variation hence a scalar dissipation close to zero ($\chi = 2D|\nabla f|^2$), that is species may react completely, eqs.11-12.

This explains the high combustion efficiency predicted and the position of the highest temperature: next to the inlet ducts. Measured CH* chemiluminescence, fig.11, does not envisage this possibility.
A too high grid refinement increases the importance of a correct description of the molecular properties of every single species and, hence, the consequent mixing rules description.
The non-premixed approach does not permit the assumption of mixing rules, so mixing transport properties are described by nitrogen transport properties, that is the species with the greatest mass fraction value.

Conclusions

This work upgrades previous work by these authors [1] simulating an air/methane micro-combustion chamber, designed and built at the Polytechnic of Milan with nominal thermal power of 125W, using RANS approach and reduced chemistry models.
Here the numerical simulation is LES, and combustion is modeled with Flamelets calculated using the GRIMech 3.0.
Two simulations are reported, differing in the wall temperature imposed: "Simulation 1" 550K while "Simulation 2" 750K.
"Simulation 2" predicts well the exhaust temperature while "Simulation 1" underpredicts it.
Both overestimate the combustion efficiency η defined above, mainly due to underprediction of the CO molar fraction at the exit.
The experimental CH* chemiluminescence mean image evidenced some differences with the flame location identified in the temperature map predictions, suggesting that flame predictions close the wall need better modeling. This is an issue that needs further investigation.
The high level of grid refinement, $y^+ \leq 1$, suggests a possible reason in the assumption that diffusivity is essentially only turbulent.
It is this assumption that makes possible to reduce the species transport equations to only one equation (in f), and eliminating molecular transport.
This simplification is valid only for high turbulence. RMS maps demonstrate this, but the grid is so fine that predicted turbulent properties are much lower than molecular ones.
Thus to improve predictions, possible strategies may be:

1. to use a coarser grid;
2. to solve transport equations for all species.

Surely, future efforts must focus on more accurate wall temperatures and methane concentrations measurements, unavailable in the work presented, and possibly on gas-wall radiative heat transfer analysis.

References

1. Minotti, A., Bruno, C. and Cozzi, F. Numerical Simulation of a Micro-Combustion Chamber. AIAA Aerospace Science Meeting and Exhibit, AIAA-2009-0447, Orlando, FL, 2009.
2. W.-W. Kim and S. Menon. Application of the localized dynamic subgrid-scale model to turbulent wall-bounded ows. *Technical Report* AIAA-97-0210, American Institute of Aeronautics and Astronautics, 35th Aerospace Sciences Meeting, Reno, NV, January 1997.
3. S.-E. Kim. Large eddy simulation using unstructured meshes and dynamic subgridscale turbulence models. *Technical Report* AIAA-2004-2548, American Institute of Aeronautics and Astronautics, 34th Fluid Dynamics Conference and Exhibit, June 2004.
4. J. Smagorinsky. General Circulation Experiments with the Primitive Equations. I. *The Basic Experiment*. *Month. Wea. Rev.*, 91:99-164, 1963.
5. D. K. Lilly. A Proposed Modification of the Germano Subgrid-Scale Closure Model. *Physics of Fluids*, 4:633-635, 1992.
6. M. Germano, U. Piomelli, P. Moin, and W. H. Cabot. Dynamic Subgrid-Scale Eddy Viscosity Model. *Summer Workshop, Center for Turbulence Research*, Stanford, CA, 1996.
7. H. Werner and H. Wengle. Large-Eddy Simulation of Turbulent Flow Over and Around a Cube in a Plate Channel. *Eighth Symposium on Turbulent Shear Flows*, Munich, Germany, 1991.
8. Y. R. Sivathanu and G. M. Faeth. Generalized State Relationships for Scalar Properties in Non-Premixed Hydrocarbon/Air Flames. *Combustion and Flame*, 82:211-230, 1990.
9. K. N. Bray and N. Peters. Laminar Flamelets in Turbulent Flames. A. Libby and F. A. Williams, editors, *Turbulent Reacting Flows*, pages 63-114. Academic Press, 1994.
10. N. Peters. Laminar Diffusion Flamelet Models in Non Premixed Combustion. *Prog.Energy Combust. Sci.*, 10:319-339, 1984.
11. N. Peters. Laminar Flamelet Concepts in Turbulent Combustion. *21st Symp. (Int'l.) on Combustion*, pages 1231-1250, The Combustion Institute, 1986.
12. G. Dixon-Lewis. Structure of Laminar Flames. *23rd Symp. (Int'l.) on Combustion*, pages 305-324, The Combustion Institute, 1990.
13. H. Pitsch and N. Peters. A Consistent Flamelet Formulation for Non-Premixed Combustion Considering Differential Diffusion Effects. *Combustion and Flame*, 114:26-40, 1998.
14. H. Pitsch, H. Barths, and N. Peters. Three-Dimensional Modeling of NOx and Soot Formation in DI-Diesel Engines Using Detailed Chemistry Based on the Interactive Flamelet Approach. *SAE Paper* 962057, SAE, 1996.
15. J. S. Kim and F. A. Williams. Extinction of Diffusion Flames with Non-Unity Lewis Number. *Eng. Math*, 31:101-118, 1997.
16. GRI-Mech Version 3.0 released 11/16/94, http://diesel.fsc.psu.edu/~gri_mech.
17. Spalart, R. P. Direct simulation of a turbulent boundary layer up to R_θ=1410, *J. Fluid Mech.*, 187, pp. 61-98 (1988).
18. Kim, J., Moin, P., Moser, R. Turbulence statistics in fully developed channel flow at low Reynolds number, *J.Fluid Mech.*, 177, 133-166 (1987).
19. A. J. Chorin. Numerical solution of Navier Stokes equations. *Mathematics of Computation.* 22: 745-762, 1968.
20. FLUENT handbook, chapter 25.1.1.
21. Vandoormaal, J.P., and Raithby, G.D. Enhancements of the SIMPLE Method for Predicting Incompressible Fluid Flows. *Numer. Heat Transfer*, 7:147-163, 1984.
22. FLUENT handbook, chapter 25.4.3, 25-28.
23. B.P. Leonard. The ULTIMATE conservative difference scheme applied to unsteady one-dimensional advection. *Comp. Methods Appl. Mech. Eng.*, 88: 17-74, 1991.
24. Van Leer, B. Toward the Ultimate Conservative Difference Scheme. IV. A second order Sequel to Godunov's Method. *Journal of Computational Physics*, 32: 101-136, 1979.

25. F. Cozzi, A. Coghe, A. Olivani, M. Rogora. Stability and Combustion Efficiency of a Meso-Scale Combustor Burning Different Hydrocarbon Fuels. *30th Meeting of the Italian Section of the Combustion Institute*, Ischia, Italy, June 21-22, 2007.
26. Cozzi F., Coghe A., D'Angelo Y., Renou B., Boukhalfa M., Experimental study of performances and internal flow field of a meso-scale vortex-combustor, 4th European Combustion Meeting, Vienna, Austria, April 14-17, 2009.
27. Najm, H. N., Paul, P. H., Mueller, C. J., Wyckoff, P. S. On the Adequacy of Certain Experimental Observables as Measurements of Flame Burning Rate, *Comb and Flame* 113:3, pp. 312-332 (1998).